Modeling and Design Optimization of Loosely Coupled PCB Spiral Coils in Inductive Power Transfer Systems

Xiaotong Du, *Student Member, IEEE*, and Drazen Dujic, *Senior Member, IEEE*

***Abstract*—There are various possibilities to realize coil winding designs for an inductive power transfer system. In order to achieve high power transfer efficiency and power density and explore tradeoffs between the two, design optimization around the coil link is needed and often requires multiphysics modeling. In addition, the speed of optimization depends on the models complexity and used tools. This article proposes a systematic design optimization flow, which achieves fast optimization by avoiding calling finite-element method simulations in each optimization iteration. The optimization flow utilizes electric circuit model, the electromagnetic model and the thermal model. The electromagnetic models used to predict inductances, coupling and losses of coils are pretrained artificial neural networks. The temperature rise is modeled with thermal nodal networks. The electric circuit model calculates the efficiency and output voltage of each coil design. The multiphysics models are all implemented into MATLAB optimization tool. In the end, one optimal design is prototyped and developed models have been verified experimentally.**

***Index Terms*—Data driven modeling, inductive power transfer (IPT), PCB spiral coil.**

I. INTRODUCTION

IN ORDER to achieve high power transfer efficiency of the inductive power transfer (IPT) system, detailed design optimization of IPT coils is necessary. The Pareto front that shows the tradeoff between power density and the power transfer efficiency [1] is suitable to quantitatively compare the performance of different IPT coil designs. For a coil link with compensation network, the optimization could be done in different ways. Bosshard et al. [1] assumed quality factors Q and a nominal coupling factor k first and define the optimal load factor $\alpha_{\text{load}} = \frac{R_{\text{load}}}{\omega L_s}$ to achieve high efficiency. With the load factor and operation frequency, the secondary coil inductance L_s is determined. The primary coil inductance L_p can be calculated with L_s and the input and output voltage ratio. Different coil designs, which could achieve required coil characteristics L, k, and Q, are explored and compared. However, it may not always be possible to reach the optimal inductance values and coupling factor k. The optimization could be done in an alternative approach without assumptions of k and Q and without the need to predefine the coil inductance. As discussed in [2], the characteristics L, Q, and k are calculated or simulated for the coils in the entire coil size design range, and the feasible designs are only filtered out at the last step by the circuit voltage transfer ratios. Those feasible designs are compared and the optimal designs yield the final Pareto front.

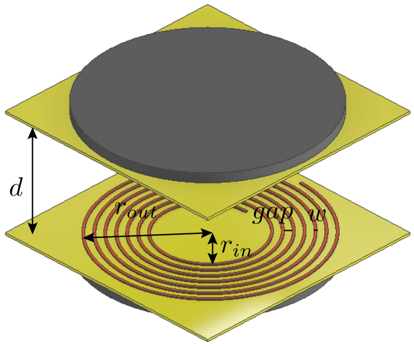

Fig. 1. PCB coil pairs with ferrite plates on their backside. r_{out} is the outer radius of windings, r_{in} is the inner radius of windings, w is the width of winding turns, gap is the gap between two adjacent turns, d is the distance between two coils. PCBs can be round shape, but are manufactured here in square shape.

In an optimization flow, accurate electromagnetic models, the electric circuit model as well as the thermal model are needed. The electromagnetic models predict characteristics including L, Q, and k of a coil pair with their winding geometries as inputs. The current and voltage in the primary and secondary sides are calculated with electric circuit model based on the electric specifications and coil characteristics. With the calculated current, the loss of the coils can be obtained from electromagnetic models and the thermal model is needed to predict the temperature rise in the coil pairs.

An accurate electromagnetic model is complex especially for a loosely coupled system where a large air gap is present in the magnetic path, as shown in Fig. 1. A typical application where a large air gap is needed is where high insulation capability is required between the primary and secondary coils, such as auxiliary power supply (APS) for medium voltage converters [3]. Chen et al. [4] modeled the impedance of planar transformers with small air gaps on the magnetic path under

---

Manuscript received 13 April 2023; revised 18 July 2023; accepted 14 August 2023. Date of publication 17 August 2023; date of current version 22 September 2023. Recommended for publication by Associate Editor Ming Liu. *(Corresponding author: Xiaotong Du.)*

The authors are with the Power Electronics Laboratory, École Polytechnique Fédérale de Lausanne, 1015 Lausanne, Switzerland (e-mail: xiaotong.du@epfl.ch; drazen.dujic@epfl.ch).

Color versions of one or more figures in this article are available at https://doi.org/10.1109/TPEL.2023.3306178.

Digital Object Identifier 10.1109/TPEL.2023.3306178

Ampere's Law. In order to model the flux distribution around loosely coupled coils with large air gap, the method of current images is proposed to model the field distribution by replacing the magnetic substrate with another image current. However, this is under the assumption that the magnetic slab is semi-infinite [5]. Even though the effect of finite thickness of magnetic substrate on planar inductors is adapted [6], [7], the magnetic substrate is still assumed to have infinite large surface area. The work of authors presented in [8] and [9] models the mutual inductance of loosely coupled coils based on the method of current images, however, the ferrite plate needs to be twice as large as the outermost radius of winding to be able to neglect flux leakage due to the fringing effect of the plate. When the ferrite surface is as small as the winding surface, with a large gap between primary and secondary windings, the crowded field around ferrite corners cause large error in the method of current images. So far finite-element method (FEM) simulation [10] or finite-element analysis with an integration over the entire system [11] are usually needed to model the flux distribution as well as to predict coil characteristics, such as inductance and resistance. Liu et al. [12] build the model by using FEM to obtain additional compensation coefficient to modify the method of current images. In [10] and [13], FEM is directly used to simulate and evaluate the coil pair characteristics.

FEM can be directly implemented into optimization flow to predict coil magnetic characteristics as discussed in [13], [14], and [15], which typically means that FEM would be called in each optimization iteration step. When the design requirement changes, design optimization would need to rerun FEM simulation multiple times to generate new optimization designs. Since FEM simulation is the most time-costly stage in the design procedure, if the data-base from FEM simulation can be well saved for later-on optimization over coils, the model can be quickly called and time would be significantly saved for design optimization. Recent advances of artificial intelligence makes it effective in modeling nonlinear problems,such as distributed flux around IPT coils. Liu et al. [16] have optimized double-D coils with data-driven method by modeling the constant outputs ratios when there is coil misalignment with artificial neural network (ANN). With the ANN model, the design process can be accelerated significantly.

An accurate thermal model is necessary to predict the temperature rise in coils. The thermal dissipation is widely researched in the high-power application, such as EV [17]. For IPT as APS system, small surface area and dielectric encapsulation (if used) bring more challenges to the thermal coordination. The thermal model can be obtained by FEM and thermal network method (TNM). Thermal FEM needs the supporting of computational fluid dynamics (CFD) to extend the constant convection coefficients on the boundary with an explicit simulation of the fluid flow around the object and it is computationally expensive. TNM sacrifices modeling accuracy with fast model execution. But for the symmetrical geometry, the accuracy with TNM is relatively high. In addition, comparing with FEM, TNM model is easier to be integrated in the optimization flow.

In this article, electromagnetic models based on ANN network and a TNM model are proposed, which are adaptable for various coil geometries. These models, together with electric circuit models [18], are later integrated into the genetic algorithm (GA) to optimize loosely coupled IPT coil link achieving high power density and high efficiency while within thermal limit. The entire optimization algorithm and all the models involved are exclusively based on MATLAB scripts and do not need to run external simulations, such as FEM or circuit simulations during the optimization iterations, which permits fast optimization.

TABLE I
DESIGN SPECIFICATIONS

V_{in}	V_{out}	V_{ins}	P_{out}	$f_s w$
80 V	$36 \pm 2V$	6 kV	130 W	500 kHz

TABLE II
DESIGN SPACE OF PCB COIL GEOMETRIES

Features	Characteristics	Value/Range	Units
Outer radius	$r_{\text{out}p}, r_{\text{out}s}$	< 90	mm
Inner radius	$r_{\text{in}p}, r_{\text{in}s}$	> 0	mm
Trace width	w_p, w_s	< 10	mm
gap-width ratio	$\text{gwr}_p, \text{gwr}_s$	< 1.5	-

This article optimizes IPT coil designs as APS for medium voltage converters, whereas the optimization flow can be easily generalized to other applications with datasets extensions. The rest of this article is organized as follows. In Section II, fixed system specifications as well as design space of winding geometries are discussed. Section III shows the details of building ANN models from electromagnetic FEM simulation datasets. In Section IV electric circuit models for the coil link with compensation network is presented. Section V builds a 2-D thermal network for the enclosured coil system. Later these models are implemented into optimization tool to generate Pareto fronts of coil winding geometries in Section VI. In the end, one design is selected on the Pareto front and tested to verify the accuracy of models in Section VII. Finally, Secion VIII concludes this article.

II. SYSTEM SPECIFICATIONS

The system specifications are listed in Table I, which are initially explained in [2]. PCB winding is chosen due to its easy and accurate manufacturing. The round spiral coil is used because of its high power density when compared with other shapes [19]. A 5 mm thick round shape ferrite plate, which covers the winding surface area is placed on the coil's backside to achieve better coupling performance, as shown in Fig. 1. In addition, the ferrite plate shields the leakage electromagnetic field and no metallic shielding is further placed in the coil system in this work. The ferrite material 3F36 is used due to its suitability for operating frequency up to 1 MHz, high saturation flux density B_s reaching 420 mT at 100 °C, and a flat losses responses over a wide temperature range from 0 °C to 120 °C.

The winding geometries are free parameters in design, and its design space is given in Table II. Considering the construction of the MV converter power stages, the outer radius of coil size is constrained. In our application, 80 mm is set as the maximum outer radius of spiral coils. A large trace width causes high ac resistances of PCB trace, and therefore in this article, 10 mm is chosen as the maximum trace width. The models are built for the winding geometries in this design space.

III. COIL CHARACTERISTICS MODELS BASED ON ANN

The magnetic model of the loosely coupled PCB coils predicts its self-inductance, mutual inductance, winding resistance, and core losses. The existing analytic models for PCB coils are either for small air gap between primary and secondary coils [20], or for the coils with relatively large ferrite [21], [22], or analytic modeling for coils without ferrite [23], [24]: when no magnetic shielding is added in the system, Neumann formula can be used to predict the inductance of the system. For loosely coupled PCB-based IPT coils, in the existing researches, the design and optimization is usually customized for one fixed set of specifications and lacks generality. To design the PCB-based IPT coils, FEM 3-D or FEM 2-D are usually employed to explore different geometry potentials [25]. In such simulation-driven optimization [26], when the new design specifications are introduced, it becomes necessary to reexecute the FEM simulations, incorporating varying geometry parameters. As an alternative approach, a factor ratio to represent the effect of ferrite on PCB coils, which is obtained from FEM, is used to modify the analytic model of the air core IPT coils. However, it is only applicable to designs with a limited number of degrees of freedom, such as those involving fixed core geometry [27]. When the core size changes with the winding geometry, this factor ratio also changes.

In this section, fully connected multilayer ANN is used to build the magnetic model to predict the characteristics of coil pairs. The input of ANN are coil geometries as given in Table II. The outputs of ANN are primary and secondary inductances L_p, L_s, mutual inductance L_m, primary and secondary resistances R_p, R_s, and core loss $\hat{P}_{\text{fe}-p}$, $\hat{P}_{\text{fe}-s}$ under unity current. The training data is obtained with FEM 2-D simulation. The distance between coils is 60 mm to meet insulation criteria providing air as the only insulation gap between primary and secondary coils [2].

A. Data Preprocessing

1) Data Collection: The training data is obtained from FEM 2-D and then is used to train ANN. It is possible to build a general model for all the coil geometries in the design space with limited training data by using ANN. The training datasets cannot include every design variety, and carefully selecting training datasets can increase the accuracy of ANN model. In the 2-D design, the number of turns and distance between two coils is fixed in each simulation. In the meantime, the other geometry parameters, including turn width w, width-gap ratio gwr, and coil outer radius r_{out} are swept in the design space to generate training datasets. The design of experiments are shown in Fig. 2 following central composite design (CCD) and latin hypercube sampling design (LHSD) [28]. In total, in FEM simulation, 6000 different coil pair geometries are simulated in FEM and from there 12 000 single coil data are exported as training datasets to ANN.

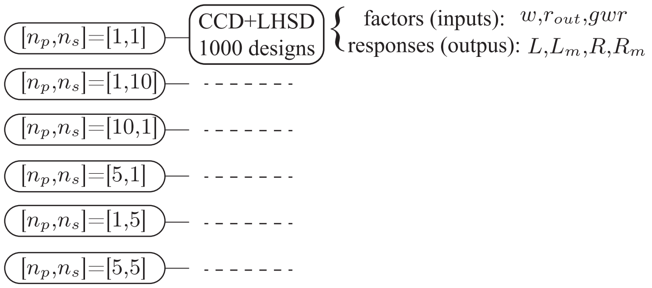

Fig. 2. In 6000 training datasets obtained with 2-D FEM simulation.

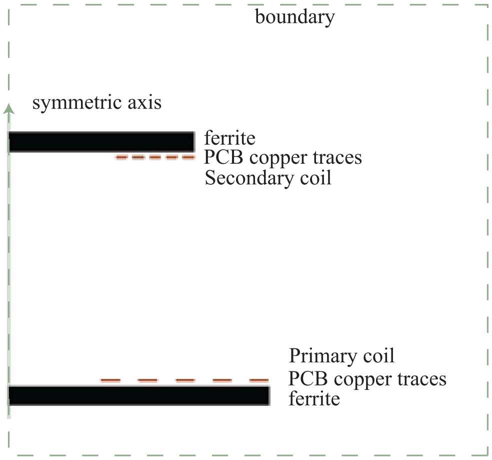

Fig. 3. Model in Ansys Maxwell 2-D with rotational symmetrical axis.

In order to speed up the simulation process with a low-computational cost, a rotational symmetry model is constructed in 2-D FEM, as shown in Fig. 3. The simulation is solved with eddy current solver. A vacuum region is built 1000 times larger than the IPT coil pair and the balloon boundary is used on the vacuum region. Current excitation is set on the cross-section surface of each turn. The initial mesh is generated automatically by Maxwell triangular adaptive uniform mesher. Tetrahedral elements are refined 30% per pass during adaptive analysis until the convergence criteria are satisfied. The adaptive process has 20 maximum number of passes, 1% energy error, and at least two converged passes as the convergence criteria.

2) Invalid Values: The coil with the geometry, which exceeds the range listed in Table II is considered as invalid value and are removed from training datasets. This reduces the training data from 12 000 to 7440.

3) Outliers: The outliers in the data is detected by applying the interquartile range rule, i.e., samples are considered as outliers outside of range $[Q_1 - 1.5\text{IQR}, Q_3 + 1.5\text{IQR}]$, where Q_1 is the first quartile and Q_3 is the third quartile through the list of all data. This reduces the training data from 7440 to 5705.

B. Feature Engineering

Ten geometrical parameters, including the parameters given in Table II and the number of turns, are input features for each model. Even though they are not fully independent from each

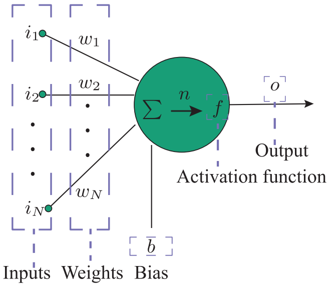

Fig. 4. Structure of the multi-input neuron. The neuron has N inputs and are denoted as $i_{1,\ldots,N}$. Each input has a weight w. The bias to the neuron is b. After executing summation operation and activation function, the neuron generates one output o.

other, for example with $r_{\text{out}-p}$, w_p, gwr_p, and n_p, $r_{\text{in}-p}$ can be derived, ten inputs features are used in order to improve the abundance of features and so to increase the ANN model accuracy. In addition, as the different features are on different scales, data for each feature is normalized into range $[-1, 1]$, which helps the models converge faster for a given learning rate.

C. *Model Implementation and Hyperparameter Tuning*

A multilayer fully connected feed-forward neural network is chosen to estimate the coil characteristics. The chosen structure is composed of one input layer, three hidden layers, and one output layer. The neuron structure is shown in Fig. 4. On each neuron, the inputs of the neuron is processed as

$$n = \sum_{j=1}^{K} w_j i_j + b. \tag{1}$$

Then, the input n passes through the activation function to generate the neuron output o, the activation function used in this work is tangent sigmoid transfer function, which is defined as

$$f(n) = \frac{2}{1 + e^{-2n}} - 1. \tag{2}$$

The back propagation algorithm first propagates the input forward through the network until getting the estimation at output. With the loss function and chain rule, the gradient of each layer is calculated backward through the network from the last to the first layer. Finally, the weights and biases are updated with gradient descent optimization rule. The mean square error between the targets and the estimation is used as the loss function (performance function) $F_{\text{loss}} = \frac{1}{N}\sum_{j=1}^{N}(T_j - O_j)^2$, which is to be minimized by adjusting the network parameters weights w and bias b.

While calculating the gradient descent vector, instead of the steepest descent algorithm, Levenberg–Marquardt is used for the update of parameters $\mathbf{x}$ [29]

$$\mathbf{x_{k+1}} = \mathbf{x_k} - [\mathbf{J^T}(\mathbf{x_k})\mathbf{J}(\mathbf{x_k}) + \mu\mathbf{I}]^{-1}\mathbf{J^T}(\mathbf{x_k})\mathbf{e}(\mathbf{x_k}) \tag{3}$$

where $\mathbf{x_{k+1}}$ are the weights and bias parameters after $k+1$ iteration, $\mathbf{x_k}$ are parameters from last iteration. $\mathbf{J}$ is the Jacobian matrix and $\mathbf{I}$ is the identity matrix. $\mathbf{e}(\mathbf{x_k})$ is a vector obtained by transferring the loss function into the form $F_{loss}(\mathbf{x}) = \mathbf{e^T}(\mathbf{x})\mathbf{e}(\mathbf{x})$. μ is the learning rate, which is updated in each iteration.

TABLE III
SPECIFICATIONS OF ANN TRAINING ALGORITHM

Training function	Levenberg–Marquardt backpropagation
Performance function	Mean squared error
Output dimensions	1
Input dimensions	10
Hidden layer size	[20, 20, 20]
Train ratio	70
Validation ratio	30

TABLE IV
ERROR ON THE TEST DATA

	L	L_m	R	$\hat{P}_{\text{fe}}$
Error	9.8%	7.3%	7.4 %	7.3%

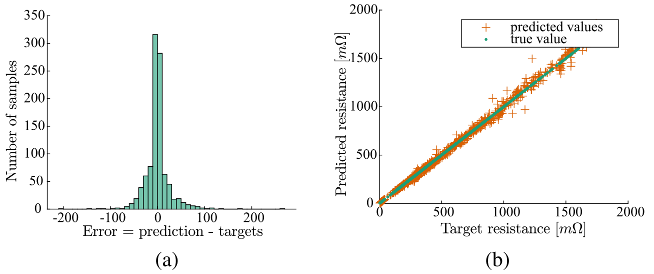

(a) (b)

Fig. 5. Performance of ANN model of resistance R on test dataset. (a) Error histogram. (b) Regression curve between the predicted response and targets.

The hyperparameters are tuned by hand, and in the end we choose: initial learning rate μ_0 to be 0.001; the decrease ratio of learning rate to be 0.1; the increase ratio of learning rate to be 10; maximum iterations to be 1000; training stops if the validation performance degrades for six consecutive iterations. In summary, the ANNs are trained with the parameters in Table III.

D. *Results*

In total, 1000 datasets are generated as test datasets with optimal space-filling design. In order to get a better performance model, the network is trained five times with the same training data, and the one with the lowest error compared with the test data is used as the final model. The mean percentage error is calculated for each model and results are given in Table IV.

Once the model is trained, the performance is evaluated with different metrics. The test datasets are fed into the trained models' input and the predicted responses are obtained from the models. Taking the model for ac resistance R as an example, the performance is shown in Fig. 5. In Fig. 5(a), the error between target values and predicted values is centered around zero and symmetrical, which means the prediction model brings almost no bias. Fig. 5(b) shows a linear fit line, where we can observe that the predicted values lie around the regression line with the regression values of 0.98.

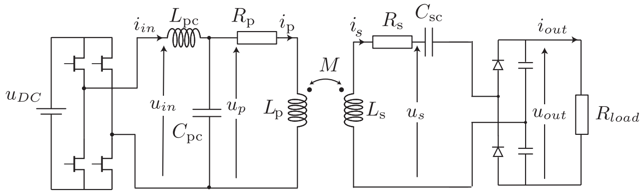

Fig. 6. IPT system composed of input DC source, full-bridge inverter, compensation network, coil link, and half-bridge rectifier.

IV. Electric Circuit Model

Adopting the LCL compensation for the primary side as shown in Fig. 6, the current through primary coil is independent of secondary side conditions [2]

$$I_p = \frac{U_{\text{in}}}{\omega L_p} \tag{4}$$

where, $\omega = 2\pi f$ is the system operating angular frequency and L_p is obtained from the ANN model. On the secondary side, with series connected capacitor, at resonant frequency, the current through the secondary coil is

$$I_s = \frac{\omega M I_p}{R_{\text{load-ac}} + R_s} \tag{5}$$

where M is the mutual inductance obtained from ANN model and $R_{\text{load-ac}}$ is the equivalent ac load. With a half-bridge rectifier, the ac load is $R_{\text{load-ac}} = 2R_{\text{load}}/\pi^2$. R_s is the secondary coil resistance and is obtained from ANN model.

The output dc voltage is

$$U_{\text{out}} = \frac{\sqrt{2}}{\pi} I_s R_{\text{load}}. \tag{6}$$

The output power on the load can be calculated as

$$P_{\text{out}} = \frac{U_{\text{out}}^2}{R_{\text{load}}}. \tag{7}$$

Both the dc and ac winding losses are proportional to the square of magnetic field and proportional to the current $P_w \propto H^2 \propto I^2$. The total winding loss is

$$P_w = r_p I_p^2 + r_s I_s^2 \tag{8}$$

where r_p and r_s are obtained from ANN model. I_p and I_s are obtained from (4) and (5).

An ANN model gives power loss in the ferrite under 1 A excitation. Loss of ferrite under nominal current is obtained using empirical Steinmetz equation [30]. This can be applied because the excitation of the coils is sinusoidal and without dc premagnetization of the material

$$P_{\text{fe}} = c_m f^x B^y \tag{9}$$

where loss density P_{fe} is in $[\frac{mW}{\text{cm}^3}]$, frequency f is in [Hz], and flux density B is in [T]. The Steinmetz parameters of the 3F36 ferrite material at frequency from 500 to 800 kHz is extracted from data sheet: $C_m = 1.12e-7, x = 2.1952, y = 2.7199$, and the temperature influence is omitted here. In (9), under constant frequency, the loss density is influenced only by magnetic flux density. The ANN model predicts the ferrite loss under 1 Arms current, when the current scales up, the magnetic flux density B scales up proportionally and therefore the ferrite loss scales up to the power y

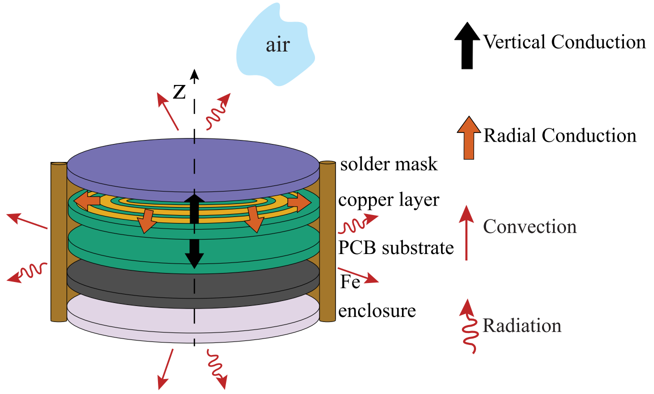

Fig. 7. Thermal flux dissipation paths in one coil.

$$P_{\text{fe}} = \hat{P}_{\text{fe}-p} I_p^y + \hat{P}_{\text{fe}-s} I_s^y. \tag{10}$$

The loss in the coil link takes windings and ferrite into consideration. The ac–ac efficiency is

$$\eta = \frac{P_{\text{out}}}{P_{\text{out}} + P_{\text{loss}}} \tag{11}$$

where $P_{\text{loss}} = P_w + P_{\text{fe}}$.

V. Thermal Model

The temperature influences the coil system performance in many ways and an accurate thermal modeling of the critical points in coil system is beneficial for coil design. Ferrite material 3F36 has low power loss from 25 °C to 100 °C. In addition, when epoxy is used, temperature influences its dielectric performance. For example, the max working temperature is around 100 °C for polyurethane and epoxy. In the coil system, heat transferred in three different ways: conduction, convection, and radiation. In our coil, there are five layers of different materials: solder mask, PCB copper, PCB substrate, ferrite, and enclosure. In each layer, the heat is transferred with horizontal heat flux as shown in Fig. 7. Between adjacent layers, the heat is transferred with vertical flux. It has to be noted that, the vertical and horizontal flux is used for simplification of modeling. On the surface of coil system, the heat exchange with air is through convection and radiation.

The thickness of each layer is fixed and is given in Table V. However the surface of each layer is varying with the winding geometry. In the following discussion, three assumptions are made to simplify the thermal model. First, the thermal contact resistance is ignored and different components are fixed together as closely as possible by applying an external force. Second, the thermal cross-coupling effects are not considered, meaning that two coils in the model are considered thermally independent. Third, the coil system is modeled as axially symmetrical structure and the modeling is only done on half-plane of the cross section, as shown in Fig. 8.

TABLE V
THICKNESS AND THERMAL CONDUCTIVITY OF DIFFERENT MATERIALS INVOLVED IN A COIL SYSTEM

Material	layer thickness [mm]	thermal conductivity [W/mK]
Solder mask	0.02	0.2
Copper (winding)	0.07	401
FR4 (PCB)	1.58	0.25
MnZn Ferrite	5	5
ABS/ASA plastic (enclosure)	2	0.14

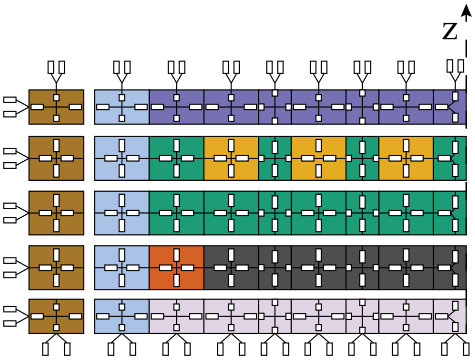

Fig. 8. Thermal network of one coil composed of five layers, from top to bottom: solder mask, PCB copper trace layer, PCB layer, ferrite layer, and plastic enclosure layer.

The entire coil is modeled as a thermal resistance network, with the ambient temperature as the boundary conditions. To predict the temperature in the planar coil, the first step is to define the thermal network, with which temperature matrix for the coil system can be predicted as

$$[T] = [T_{\text{amb}}] + [P][Z] \tag{12}$$

where Z is the admittance matrix. Given the assumptions showed above, the thermal network is based only on a half-plane of coil's cross section. The distribution of nodes depend on the coil system structure. As shown in Fig. 8, in each layer of the system, there are a row of nodes, and in each row of nodes, the number of nodes depends on the number of turns of coils. At each node, four resistances are connected to it from horizontal and vertical heat dissipation directions. The nodes are linked together by their vertical and horizontal resistances and the thermal resistance network is built. Moreover, convection and radiation resistances are attached to the surfaces of the coil.

The thermal resistance are calculated differently from conduction, convection, and radiation effects.

Conduction resistance: Inside the coils, the thermal resistances are defined by conduction effect. For the thermal conduction, at each node, four conductive resistances are built, numbered from R1 to R4 as shown in Fig. 9. The four resistances are characterized by the local geometry, including r_1: inner radius from the center of the device to the rectangle; r_2: outer radius from the center of the device to the rectangle; H: height of the rectangle that corresponds to the thickness of a device layer; L: length of the rectangle. It is computed as $L = r_2 - r_1$.

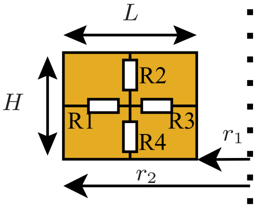

Fig. 9. Four resistances are constructed at each internal node.

R1 and R3 are radial conductive resistances

$$R1_{\text{th,cond}} = \frac{\ln(r_2/(r_1 + L/2))}{2\pi H k} \tag{13}$$

$$R3_{\text{th,cond}} = \frac{\ln((r_1 + L/2)/r_1)}{2\pi H k}. \tag{14}$$

R2 and R4 are planar conductive resistances

$$R2_{\text{th,cond}} = R4_{\text{th,cond}} = \frac{H/2}{k\pi \cdot (r_2^2 - r_1^2)}. \tag{15}$$

The summary of the materials' conductivity used in coil system is given in Table V.

Convection resistance: Thermal convection coefficient h is a number dependent on the environment conditions and object characteristics, including the air viscosity, air and object temperature, geometries, positions, materials, etc. How the coil is mounted in space will influence the convection coefficient. Taking all the environmental and object conditions into consideration, the average convection coefficient on a plane surface, h can be calculated

$$h = \frac{k_{\text{air}} N_u}{L_c} \tag{16}$$

where k_{air} is the thermal conductivity of air $[\mathrm{Wm^{-1}K^{-1}}]$ and N_u is the average Nusselt number, which represents the ratio of convective to conductive heat transfer at a boundary in the air and differentiate for hot planes facing different directions. L_c is the characteristic length of the test object. k_{air} at atmospheric pressure is dependent only on the temperature of air. The characteristic length is reflecting the object geometry and defined as the ratio between the surface area and perimeter $L_c = \frac{A}{P}$.

When the coil is vertically placed, the convection resistance from the side surfaces are

$$R_{\text{th,conv}} = \frac{1}{A_{coil} h_{coil}} = \frac{1}{h_{\text{coil}} \cdot \pi(r_2^2 - r_1^2)} \tag{17}$$

where $\pi(r_2^2 - r_1^2)$ is the local coil surface area and h_{coil} is the average convection coefficient calculated from the Nusselt number for the vertical hot plate case. For the enclosure wall, the convection thermal resistance is calculated by

$$R_{\text{th,conv}} = \frac{1}{A_{wall} h_{side}} = \frac{1}{h_{\text{side}} \cdot 2\pi r_2 \cdot H} \tag{18}$$

where $2\pi r_2 \cdot H$ is the local wall surface area and h_{wall} is the average convection coefficient calculated from the Nusselt number for the hotizontal hot plate case.

Radiation resistance: For natural cooling conditions, the radiation effect could be as more significant than the convection

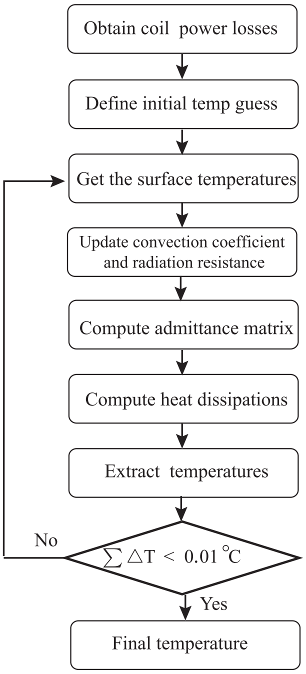

Fig. 10. Calculation flow to predict the temperature in steady state.

effect. The radiation thermal resistance is calculated as

$$R_{th,rad} = \frac{T_s - T_{amb}}{(T_s^4 - T_{amb}^4)\varepsilon\sigma A} \tag{19}$$

where A is the surface area same as the ones for the convection thermal resistance calculation, σ is the Stefan–Boltzmann constant, and ε is the emissivity coefficient of the surface, which indicates the radiation of heat from a body according to Stefan–Boltzmann law. The surface emissivity is taken as constant and under $40\,^\circ$C, being 0.9 and 0.85 for solder mask and plastic enclosure, respectively.

The heat transmission rate on the surface and the temperature on surfaces are cross dependent parameters. Convection and radiation through surface is dependent on the local surface temperature, and in reverse, the temperature on the surface is dependent on the convection and radiation rate. In the modeling, the temperature is calculated in iterations until the temperature on surfaces converge, as shown in Fig. 10. The initial temperature on the coil surfaces is set to $T_{\text{amb}} + 20^\circ$. The convection heat and radiation heat is calculated under this temperature. Through the thermal resistance network and with the knowledge of power loss in copper and ferrite, the temperature in each location of the coil system is calculated. The updated surface temperature is then used to calculate the new heat dissipation coefficients. The iteration continues until the convergence happens in five consecutive cycles. The convergence criteria is that the difference between predicted average temperature on the surface and the prediction temperature from last iteration is less than $0.01\,^\circ$C.

VI. OPTIMIZATION WITH GA

GA is used to output the Pareto fronts of optimal IPT coil pair designs for the IPT system shown in Fig. 6.

A. Objectives

The objectives of optimization are high efficiency and high power density coil link. The optimization is done for the system with specifications given in Table I. Inductances are calculated from ANN models. In order to better reflect the resistance of spiral coils, the resistance from ANN model is modified with a ratio between the length of the spiral and concentric circles, since the model is made based on 2-D FEM simulations, which use concentric circular coils rather than spiral coil. With the calculated coil characteristics, the efficiency is calculated as $\eta = \frac{P_{\text{out}}}{P_{\text{out}}+P_{\text{loss}}}$. The detailed calculation is shown in Section IV.

In addition to high efficiency, high power density is another optimization objective. For the coils meeting output power specifications, small coil size leads to high power density provided that the distance between two coils is fixed. The coil size is defined by the outer radius of two coils. Since the two coils are center aligned, the direct optimization objective is to minimize outer radius of both coils, that is minimize $\max(r_{\text{out}-p}, r_{\text{out}-s})$.

B. Constraints

The optimization is done with two constraints: output voltage range and thermal limits. Qualified output range is 36 ± 2 V. In the optimization flow, the output voltage of each design is evaluated with (6) and the designs outside of this range is filtered out. The thermal limit is defined for both primary and secondary coils. Therefore, the loss in primary and secondary coils should be separated.

The power losses of windings are

$$\begin{aligned} P_{w-p} &= r_p I_p^2 \\ P_{w-s} &= r_s I_s^2. \end{aligned} \tag{20}$$

The power losses in the ferrite are

$$\begin{aligned} P_{\text{fe}-p} &= \hat{P}_{\text{fe}-p} I_p^y \\ P_{\text{fe}-s} &= \hat{P}_{\text{fe}-s} I_s^y \end{aligned} \tag{21}$$

where $\hat{P}_{\text{fe}-p}$ and $\hat{P}_{\text{fe}-s}$ are primary and secondary core losses under 1 Arms current obtained from ANN model.

The winding loss calculated from (20) and core loss calculated from (21) are fed into the thermal model in Section V. The loss is distributed according to turns length ratio. With the input loss, the maximum temperature rise in the coil system can be calculated, and the thermal constraint is set to be $\Delta T < 80\,^\circ$C considering the stable temperature range of ferrite and insulation material.

C. Initial Generation

The initial population of GA is important to the calculation efficiency of GA. If letting the initial population be entirely random, the optimization would be slow and may end up at no feasible solutions. In order to avoid this situation, a fast brute force searching with big steps is used to provide the first population. The geometry parameters including w, r_{out}, and gwr each takes four values at even intervals across their range. Number of turns is swept from one turn to the maximum possible

TABLE VI
OPTIONS OF "GAMULTIOBJ" FUNCTION

Option	Description	Value
PopulationSize	Size of population	100
DistanceMeasureFcn	The distance function maintains diversity on a front by favoring individuals that are relatively far away on the front	@distancecrowding,'genotype'
FunctionTolerance	The algorithm stops if the average relative change in the distance of pareto front over MaxStallGenerations (= 50) generations is less than or equal to FunctionTolerance	1e-3

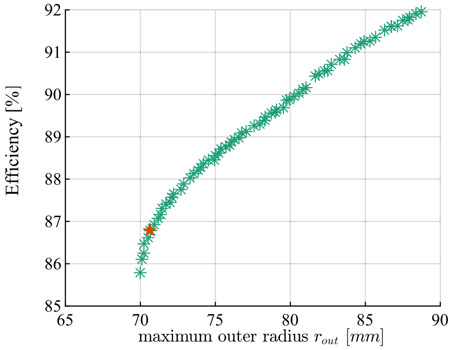

Fig. 11. Pareto front of coil designs. The prototyped design is marked with star.

turns within the coil surface. For each distance, less than 1000 designs are evaluated in the brute force stage within 3 min. The designs that fullfill the thermal limit and output voltage limit are considered as valid solutions, and are taken as the initial generation in GA optimization, based on which more generations are developed and explored.

D. Results

The optimization is done with the "gamultiobj" function in MATLAB. The main function options are given in Table VI. Other features not specified here are assigned default values in [31].

The Pareto fronts shown in Fig. 11 is generated as the result of the optimization flow. The tradeoff between small coil size and high efficiency is clearly observed. In order to verify the power transfer capability of optimization results, a turning point on the Pareto front marked with star is prototyped and tested. This coil pair has small radius below 71 mm and 87 % ac–ac power transfer efficiency. The prototyped coil pair winding geometry is given in Table VII. The primary and secondary coils has similar outer radius, which brings better coupling. For both primary and secondary sides, the trace width is below 8 mm and the space–width ratio is below 0.8. The photos of the prototyped coils are shown in Fig. 12.

VII. EXPERIMENTAL RESULTS

A. Coil Characteristics Test

The coil pair is tested with LCR meter at 500 kHz and results are listed in Table VIII together with ANN prediction results and FEM simulation results. The errors between ANN model results and test results are below 5%.

TABLE VII
PARAMETERS OF THE PROTOTYPED COILS

Specifications	Features	characteristics
primary coil		
outer radius	r_{outp}	70.70 mm
trace width	w_p	7.67 mm
turns gap	s_p	4.14 mm
turns number	n_p	3
space-width ratio	$\frac{s_p}{w_p}$	0.54
secondary coil		
outer radius	r_{outs}	70.66 mm
trace width	w_s	4.54 mm
turns gap	s_s	3.50 mm
turns number	n_s	4
space-width ratio	$\frac{s_s}{w_s}$	0.77

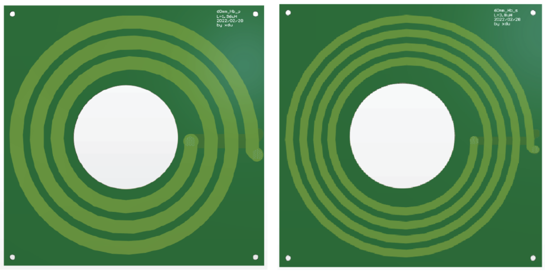

(a) (b)

Fig. 12. Prototyped coil pair. (a) Primary coil. (b) Secondary coil.

TABLE VIII
MODELING, FEM, AND TEST RESULT OF INDUCTANCE AND RESISTANCE OF THE COIL PAIR

Coil pair	$L_p[\mu H]$	$L_s[\mu H]$	$R_p[m\Omega]$	$R_s[m\Omega]$	$L_m[\mu H]$
ANN	1.97	3.82	85	172	0.56
2D FEM	1.95	3.80	84	168	0.53
Test	1.93	3.75	82	164	0.54
Error	2%	1.8%	3.6%	4.8%	3.7%

The error is the difference between modeling result and test result.

B. Power Test

The coil pair detailed in Table VII is later tested with the testbench shown in Fig. 13. The coil pair is tested with an air gap of 60 mm, nominal load of 10 Ω, input voltage of

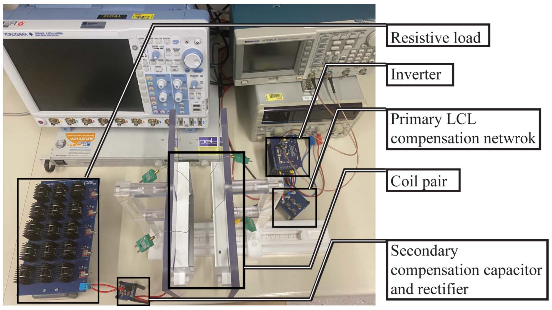

Fig. 13. Test bench of a coil pair consists of a DC power source, full-bridge inverter, the primary side compensation network, primary coil, secondary coil, the secondary side compensation network, rectifier, and resistor load.

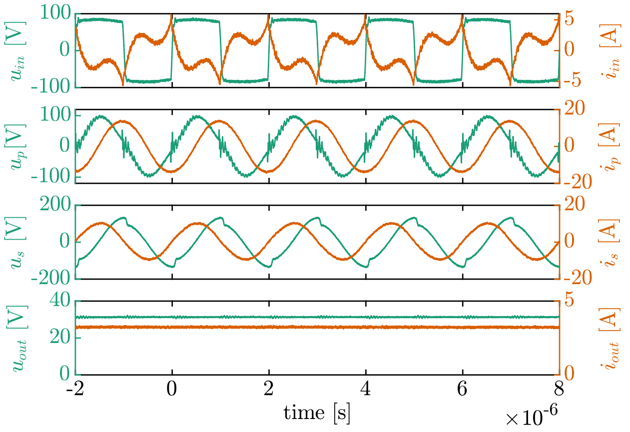

Fig. 14. Voltage and current waveform at nominal load. From top to bottom: input voltage and current between inverter and compensation network; voltage and current of the primary coil; voltage and current of the secondary coil; output DC voltage and current of load.

80 V, and operating frequency of 500 kHz. Other components in the test bench are as follows. The transmitter coil is connected to a GaN HEMTs-based full-bridge inverter (Infineon, EVAL-1EDF-G1-HB-GAN). The receiver coil is connected to Schottky diode-based passive half-bridge rectifier (ST, STPS30M100DJF). The LCL compensation network is used on primary side and series compensation network is used on secondary side. TDK MLCC capacitors are used due to low ESR. High-power high frequency inductors are used as compensation inductor.

The test results are shown in Fig. 14. With an input dc voltage of 80 V, 31.5 V is observed at dc output. The voltage before the compensation network is square shape and the current is a distorted waveform composed of fundamental and high frequency harmonics. After the compensation network, the current through the primary coil and voltage across it are sinusoidal waveforms of fundamental frequency. The induced current to the secondary side is of fundamental frequency due to the compensation capacitor on the secondary side. However the voltage across secondary coil shows a voltage jump at the current zero crossing point, which can be explained by the voltage potential change of the rectifier capacitors when the current direction changes.

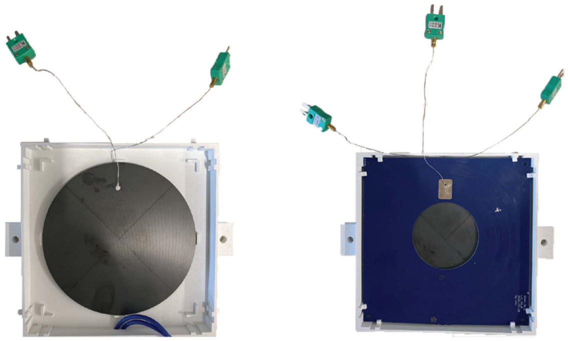

(a) (b)

Fig. 15. Prototype with thermal couples. (a) Inserted between ferrite and PCB. (b) On the top surface of PCB.

In order to verify the temperature rise is within safety limit, four thermocouples are inserted in each coil and placed on four different layers: the surface of PCB copper trace, between the PCB and ferrite, between ferrite and enclosure, and on the bottom surface of coil holder. In each layer, the thermocouple is on the most inner turn of spiral coils.

Minature thermocouples plug type K XF-1046-FAR have 0.5 mm diameter and are used to measure the surface temperatures. Thermally conductive silicon adhesive is used to fix the thermocouples between the inner surfaces (between enclosure and ferrite, and between ferrite and PCB) as shown in Fig. 15(a), and thermopads are used to fix the thermocouples on the outer surfaces (on PCB and on enclosure) as shown in Fig. 15(b). The stabilized temperature is measured and shown in Fig. 16 together with the calculated temperature from thermal network model. It can be seen that the error between the measured surface temperature and calculated surface temperature is within 3 °C. In each coil, the hottest temperature is at the copper layer. This is because most of loss in this coil system appears on the winding. The backside of the coil shows the lowest temperature and has a large temperature gap with the ferrite layer, which is due to the thick plastic wall on the backside (composed of the back coil enclosure and the coil holder).

C. Load Condition Change

The developed IPT system is supposed to serve as APS for power electronics converters, and the load condition of IPT system could change as the converter states changes. In the power test, a resistor bank is connected to the IPT as the load to imitate the converters. By switching ON and OFF resistors, the load change can be controlled. As a representation, the voltage and current at 50 Ω load is shown in Fig. 17.

A N4L PPA5530 precision power analyzer is used to analyze the dc–dc efficiency. The output voltage and power and dc–dc efficiency with different load conditions are given in Table IX. The nominal load resistor is 10 Ω. When the resistor increases

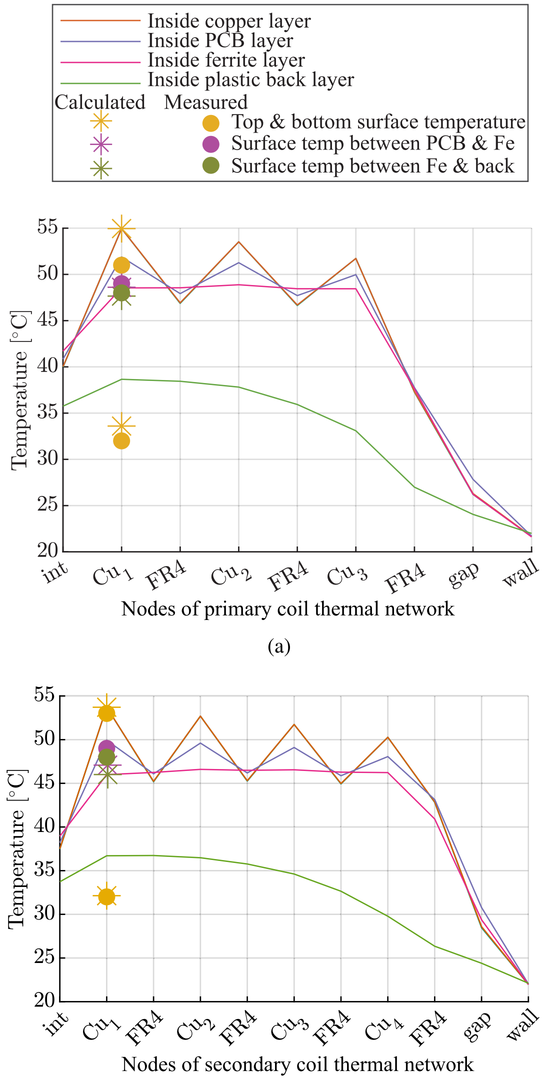

(a)

(b)

Fig. 16. Measured and calculated temperature in different layers in (a) primary coil and (b) secondary coil. Stars "*" are the calculated top and bottom surface temperature. Dots "·" are the measured surface temperature. Lines "-" are the calculated temperature at each node inside each layer.

TABLE IX
OUTPUT VOLTAGE, OUTPUT POWER, AND EFFICIENCY OF DIFFERENT LOAD CONDITIONS

Resistive load	50 Ω	25 Ω	16.7 Ω	12.5 Ω	10 Ω
Output voltage	36.26	35.43	34.56	33.65	32.82
Output power	26.88	51.23	72.97	92.08	109.42
DC-DC efficiency	0.55	0.68	0.73	0.75	0.75

five times (the load drops to 20% of nominal load), the voltage varies slightly and stays within the range [32.82–36.26 V]. The voltage source behavior of the IPT system is, therefore, verified. In addition, it can be observed that when the load drops, the power transfer efficiency drops as well, and the highest efficiency appears at nominal load condition.

The temperature in both coils are recorded while the load gradually connects to the secondary side. When the temperature is observed starting to stablize (at $t_1, \ldots t_5$), 20% more load is connected to the secondary side at each time point. As shown in Fig. 18, at initial state, the load is disconnected to the secondary coil. The temperature on the secondary side is not rising due to negligible power loss on the secondary side, however temperature on the primary coil rises rapidly.

When the load increases from no load to full load by adding 20% each time, the secondary side coil becomes hotter at each time point due to higher loss, and the load change can be clearly seen in the temperature rise pattern in secondary coils. However,

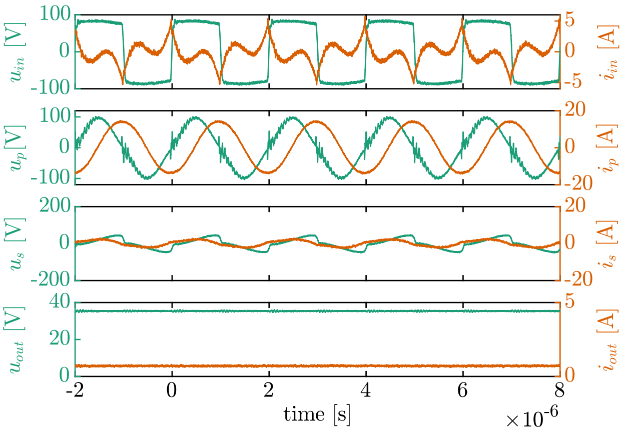

Fig. 17. Voltage and current waveform at 50 Ω load. From top to bottom: input voltage and current between inverter and compensation network; voltage and current of the primary coil; voltage and current of the secondary coil; output DC voltage and current of load.

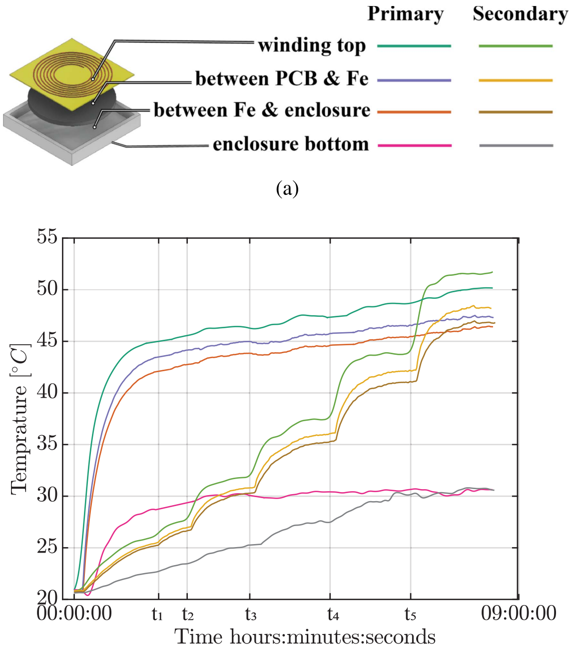

(a)

(b)

Fig. 18. Temperature rise in both coils in different layers. The load is disconnected with the secondary coil at initial state. (a) The illustration of thermal couple positions. (b) Recorded temperature. From time t_1 to t_5, the load connection rises from 20%, 40%, 60%, and 80% to full load.

TABLE X
KEY COMPONENTS IN THE IPT SYSTEM

Components	Parts number	Quantity
primary side inverter transistors	GaN IGOT60R070D1	8
primary side compensation inductor L_{pc}	Wurth Elektronik WE-HCF 7443320068, 0.68 µH	2
	TDK SPM10040T-R47M-HZ 0.47 µH	2
primary side compensation capacitor C_{pc}	NP0 ceramic capacitor 22 nF	8
secondary side compensation capacitor C_{sc}	NP0 ceramic capacitor 6.8 nF	4
secondary side rectifier diodes	power Schottky diodes STPS30M100DJF	4

the temperature of primary side slowly increases $5\,^{\circ}$C from no load to full-load condition. This verifies again that the current through primary coil is independent of load condition.

D. Loss Decomposition Analysis

In the design process of IPT coils, the losses on the inverter, rectifier, and compensation networks are neglected, and this leads to the difference of the measured dc–dc efficiency and predicted ac–ac efficiency. The components used in the IPT power transfer link are listed in Table X. The loss analysis of those components is done with the measured waveform in Fig. 14. The primary side inverter is a full bridge inverter. In each leg, there are two 600 V GaN transistors in parallel to reach the high current capability. In total, eight GaN transistor are in the inverter stage. The primary side compensation inductance is composed of four inductors connected in series to reach 2.3μH in total. The primary compensation capacitor is composed of eight multilayer ceramic capacitors of 22 nF. Four branches of capacitors are in parallel to increase current capability and in each branch there are two capacitors connected in series.

1) *GaN devices losses:* The inverter works with fixed duty cycle at 0.5. The GaN transistors in the inverter operation has conduction loss, reverse conduction loss, switching losses, and gate driving losses. The conduction losses, reverse conduction loss, and gate driving losses are calculated following the application note [32]. Due to the ZVS at turn-ON, GaN in the rectifier has only turn-OFF losses as switching losses. The turn-OFF losses is characterized through test by capturing the voltage and current over one GaN device under nominal operation.
2) *Compensation network losses:* The primary side compensation inductor is composed of two inductors of 0.68 μH from Wurth Elektronik and two inductors of 0.47 μH from TDK. There are two purposes of selecting these components: first, to achieve the total inductance value that is closest to the desired compensation inductance; second, to have low losses at the nominal operating point. Loss of two inductors at 0.68 μH from Wurth Elektronik can be calculated by its loss tool [33]. Two inductors from TDK have quality factor at 500 kHz to be 83.5, quality factor at 1.5 MHz is 56.4, and at 2.5 MHz is 51.2. The losses on these two inductors are calculated with its quality factors. The loss on NP0 ceramic capacitors are calculated with its dissipation factor $DF \approx 0.1\%$.
3) *Rectifier diode losses:* In each branch, there are two diodes in parallel. In total, there are four Shottky diodes STPS30M100DJF of rating 100 V, 30 A are used. At $125\,^{\circ}$C junction temperature, $U_f = 0.4 + 0.015 \cdot I_f$.

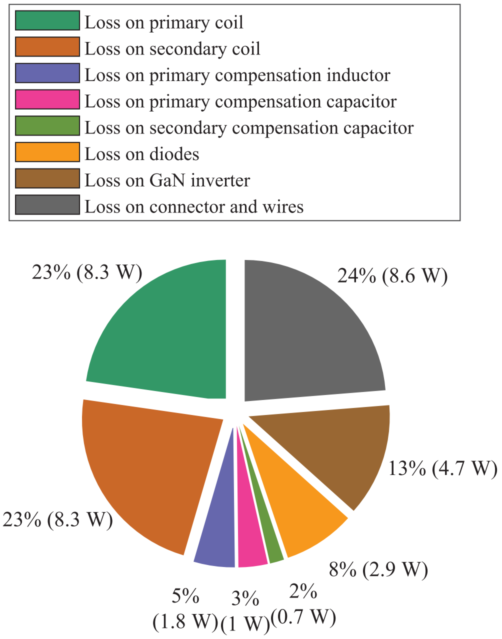

Fig. 19. Losses distribution in the prototyped IPT system at nominal operation point.

4) *Connector and wire losses:* In addition to the losses on coil pair, GaN switches, compensation networks and diodes, there are losses on the connector and wires, which also play an important role in high-frequency operation. This loss is obtained by deducting other losses from the total loss

$$P_{\mathrm{other}} = P_{\mathrm{in}} - P_{\mathrm{out}} - P_{\mathrm{GaN}} - P_{\mathrm{ind}} - P_{Cp} - P_{Cs} - P_{\mathrm{dio}} - P_{\mathrm{coil}}. \tag{22}$$

The test waveform at nominal load is taken into calculation of losses. The prototyped IPT system achieves 75% dc–dc efficiency. The loss decomposition is shown in Fig. 19. The losses on coils count 46% of total loss. In addition to that, the losses on connectors and wires are the second largest loss, which count 24% of total loss. Other losses mainly appear on GaN devices, on diodes and on primary compensation inductors. Further efficiency improvement can be achieved by optimizing wire layouts and paralleling components.

VIII. CONCLUSION

This article proposes three models for loosely coupled PCB-based IPT coil: an magnetic modeling method based on ANN and FEM simulation data; a electric circuit model for IPT with the LCL-S compensation network; a thermal model based on thermal network. The three models are fully MATLAB based and are integrated into the optimization tool, which optimizes coil geometry fast without calling external simulations. The magnetic model predicts coil link characteristics including coil inductance, winding resistance, and core losses for coil pairs with arbitrary winding geometries. The electric model calculates the power transfer efficiency and IPT outputs based on coil characteristics and system specifications. The thermal model predicts the temperature rise in each component in the coil enclosure.

The models proposed in this manuscript have the following advantages. The proposed magnetic model can be easily integrated into the optimization tool and can realize fast computation of arbitrary winding geometry without using FEM. When the optimization specification changes, the inductances and resistances of new optimal designs can be explored rapidly without extra simulation effort.

The proposed thermal network model takes into consideration both the axial and the radial directions. In addition, due to the coupling between the surface temperature and the convection and radiation resistances, the convection and radiation resistances are updated at each iteration while predicting the temperature until convergence is reached, resulting in higher accuracy. Furthermore, the thermal network model is computationally fast and easy to implement into optimization tool compared to CFD simulations or hybrid methods.

Multiphysics models are implemented to optimize winding geometries to achieve high efficiency and high power density IPT coil link while meeting thermal limits. As a demonstration, the optimization is done with the electric specifications defined for an APS system in MV converters and the prototyped PCB coil pair achieves 75% dc–dc efficiency. Moreover, this optimization flow is capable to be generalized to other applications.

ACKNOWLEDGMENT

The authors would like to thank Mr. Jérémie Veuthey for his contributions on thermal modeling of coils.

REFERENCES

[1] R. Bosshard, J. Mühlethaler, J. W. Kolar, and I. Stevanović, "The η-α-Pareto front of inductive power transfer coils," in *Proc. 38th Annu. Conf. IEEE Ind. Electron. Soc.*, 2012, pp. 4270–4277.

[2] X. Du, C. Li, and D. Dujić, "Design and characterization of PCB spiral coils for inductive power transfer in medium-voltage applications," *IEEE Trans. Power Electron.*, vol. 37, no. 5, pp. 6168–6180, May 2022.

[3] S. Zhao et al., "A 4 kV/120 a SiC solid-state DC circuit breaker powered by a load-independent IPT system," *IEEE Trans. Ind. Appl.*, vol. 58, no. 1, pp. 1115–1125, Jan. 2022.

[4] M. Chen, M. Araghchini, K. K. Afridi, J. H. Lang, C. R. Sullivan, and D. J. Perreault, "A systematic approach to modeling impedances and current distribution in planar magnetics," *IEEE Trans. Power Electron.*, vol. 31, no. 1, pp. 560–580, Jan. 2016.

[5] W. Roshen and D. Turcotte, "Planar inductors on magnetic substrates," *IEEE Trans. Magn.*, vol. 24, no. 6, pp. 3213–3216, Nov. 1988.

[6] W. Roshen, "Effect of finite thickness of magnetic substrate on planar inductors," *IEEE Trans. Magn.*, vol. 26, no. 1, pp. 270–275, Jan. 1990.

[7] K. O'Donoghue and P. Cantillon-Murphy, "Planar magnetic shielding for use with electromagnetic tracking systems," *IEEE Trans. Magn.*, vol. 51, no. 2, Feb. 2015, Art. no. 8500112.

[8] W. Hurley and M. Duffy, "Calculation of self- and mutual impedances in planar sandwich inductors," *IEEE Trans. Magn.*, vol. 33, no. 3, pp. 2282–2290, May 1997.

[9] Y. P. Su, X. Liu, and S. Y. R. Hui, "Mutual inductance calculation of movable planar coils on parallel surfaces," *IEEE Trans. Power Electron.*, vol. 24, no. 4, pp. 1115–1123, Apr. 2009.

[10] T. Diekhans and R. W. De Doncker, "A dual-side controlled inductive power transfer system optimized for large coupling factor variations and partial load," *IEEE Trans. Power Electron.*, vol. 30, no. 11, pp. 6320–6328, Nov. 2015.

[11] Y. Otomo and H. Igarashi, "A 3-D topology optimization of magnetic cores for wireless power transfer device," *IEEE Trans. Magn.*, vol. 55, no. 6, Jun. 2019, Art. no. 8103005.

[12] H. Liu, J. Xie, S. Yang, C. Zhu, X. Zhang, and F. Lu, "A general data-driven design methodology of magnetic couplers for wireless power transfer systems," in *Proc. 48th Annu. Conf. IEEE Ind. Electron. Soc.*, 2022, pp. 1–6.

[13] R. Bosshard and J. W. Kolar, "Multi-objective optimization of 50 kW/85 kHz IPT system for public transport," *IEEE Trans. Emerg. Sel. Topics Power Electron.*, vol. 4, no. 4, pp. 1370–1382, Dec. 2016.

[14] Z. Luo, X. Wei, M. G. S. Pearce, and G. A. Covic, "Multiobjective optimization of inductive power transfer double-d pads for electric vehicles," *IEEE Trans. Power Electron.*, vol. 36, no. 5, pp. 5135–5146, May 2021.

[15] S. Inoue, R. Nimri, A. Kamineni, and R. Zane, "A new design optimization method for dynamic inductive power transfer systems utilizing a neural network," in *Proc. IEEE Energy Convers. Congr. Expo.*, 2021, pp. 1496–1501.

[16] H. Liu, J. Xie, S. Yang, C. Zhu, X. Zhang, and F. Lu, "A general data-driven design methodology of magnetic couplers for wireless power transfer systems," in *Proc. 48th Ann. Conf. IEEE Ind. Electron. Soc.*, 2022, pp. 1–6.

[17] B. Zhang et al., "Multi-objective thermal optimization based on improved analytical thermal models of a 30 kW IPT system for EVs," *IEEE Trans. Transport. Electrific.*, vol. 9, no. 1, pp. 1910–1926, Mar. 2023.

[18] X. Du and D. Dujić, "Inductive power transfer system with series connected primary and independent secondary coils," in *Proc. 46th Annu. Conf. IEEE Ind. Electron. Soc.*, 2020, pp. 3901–3906.

[19] R. Bosshard, J. Mühlethaler, J. W. Kolar, and I. Stevanović, "Optimized magnetic design for inductive power transfer coils," in *Proc. 28th Annu. IEEE Appl. Power Electron. Conf. Expo.*, 2013, pp. 1812–1819.

[20] S. Jeong et al., "Smartwatch strap wireless power transfer system with flexible PCB coil and shielding material," *IEEE Trans. Ind. Electron.*, vol. 66, no. 5, pp. 4054–4064, May 2019.

[21] W. Hurley and M. Duffy, "Calculation of self and mutual impedances in planar magnetic structures," *IEEE Trans. Magn.*, vol. 31, no. 4, pp. 2416–2422, Jul. 1995.

[22] S. Kim et al., "High-efficiency PCB- and package-level wireless power transfer interconnection scheme using magnetic field resonance coupling," *IEEE Trans. Compon. Packag. Manuf. Technol.*, vol. 5, no. 7, pp. 863–878, Jul. 2015.

[23] T. Imura and Y. Hori, "Maximizing air gap and efficiency of magnetic resonant coupling for wireless power transfer using equivalent circuit and Neumann formula," *IEEE Trans. Ind. Electron.*, vol. 58, no. 10, pp. 4746–4752, Oct. 2011.

[24] B. J. Varghese, T. Smith, A. Azad, and Z. Pantic, "Design and optimization of decoupled concentric and coplanar coils for WPT systems," in *Proc. IEEE Wireless Power Transfer Conf.*, 2017, pp. 1–4.

[25] A. Ramezani and M. Narimani, "An efficient PCB based magnetic coupler design for electric vehicle wireless charging," *IEEE Open J. Veh. Technol.*, vol. 2, pp. 389–402, 2021.

[26] Y. Fang, J. Qu, B. M. H. Pong, C. K. Lee, and R. S. Y. Hui, "Quasi-static modeling and optimization of two-layer PCB resonators in wireless power transfer systems for 110-kV power grid online monitoring equipment," *IEEE Trans. Ind. Electron.*, vol. 69, no. 2, pp. 1400–1410, Feb. 2022.

[27] A. L. F. Stein, P. A. Kyaw, and C. R. Sullivan, "Wireless power transfer utilizing a high-*q* self-resonant structure," *IEEE Trans. Power Electron.*, vol. 34, no. 7, pp. 6722–6735, Jul. 2019.

[28] B. Jones and D. C. Montgomery, *Design of Experiment: A Modern Approach*. Hoboken, NJ, USA: Wiley, Nov. 2019.

[29] K. Levenberg, "A method for the solution of certain non-linear problems in least squares," *Quart. Appl. Math.*, vol. 2, no. 2, pp. 164–168, 1944.

[30] C. Steinmetz, "On the law of hysteresis," *Proc. IEEE*, vol. 72, no. 2, pp. 197–221, Feb. 1984.

[31] "Gamultiobj," Accessed: Apr. 12, 2023. [Online]. Available: https://ch.mathworks.com/help/gads/gamultiobj.html

[32] B. Zojer, "Infineon application note: Driving coolgan 600 V high electron mobility transistors," Tech. Rep. AN_PL52, May 3, 2018.

[33] "Würth elektronik redexpert," Accessed: Apr. 12, 2023. [Online]. Available: https://redexpert.we-online.com/we-redexpert/en/#/redexpert-embedded

Xiaotong Du (Student Member, IEEE) received the B.Sc. and M.Sc degrees in electrical engineering from Xi'an Jiaotong University, Xi'an, China, in 2016 and 2019, respectively. During the B.Sc. degree, she spent two years at École Centrale de Nantes, Nantes, France, as an double degree program student and received Dipl.-Ing degree. She is currently working toward the Ph.D. degree at École Polytechnique Fédérale de Lausanne (EPFL), Lausanne, Switzerland.

In 2019, she joined Power Electronics Laboratory, EPFL, as a Doctoral Research Assistant. Her research interests include modeling, design, and optimization of inductive power transfer systems.

Drazen Dujic (Senior Member, IEEE) received the Dipl.-Ing. and M.Sc. degrees in electrical engineering from the University of Novi Sad, Novi Sad, Serbia, in 2002 and 2005, respectively, and the Ph.D. degree in electrical engineering from Liverpool John Moores University, Liverpool, U.K., in 2008.

From 2002 to 2006, he was with the Department of Electrical Engineering, University of Novi Sad, as a Research Assistant. From 2006 to 2009, he was with Liverpool John Moores University, as a Research Associate. From 2009 to 2013, he was with the ABB Corporate Research Centre, Switzerland, as the Principal Scientist, working on the power electronics projects spanning the range from low-voltage/power SMPS in below kilowatt range to medium voltage high-power converters in a megawatt range. From 2010 to 2011, he was a member of a project team responsible for the development of the world's first power electronic traction transformer successfully commissioned on the locomotive. From 2013 to 2014, he was with ABB Medium Voltage Drives, Turgi, Switzerland, as a Research and Development Platform Manager, responsible for ABB's largest IGCT-based medium voltage drive ACS6000. He is currently with the École Polytechnique Fédérale de Lausanne (EPFL), Lausanne, Switzerland, as an Associate Professor and the Director of the Power Electronics Laboratory. He has authored or coauthored more than 200 scientific publications and has filed 20 patents. His research interests include the areas of design and control of advanced high-power electronics systems for medium voltage applications.

Dr. Dujic was the recipient of the First Prize Paper Award from the Electric Machines Committee of the IEEE Industrial Electronics Society, in 2007. In 2014, he has received the Isao Takahashi Power Electronics Award for outstanding achievement in power electronics, and in 2018, the EPE Outstanding Service Award from the European Power Electronics and Drives Association. He is an Associate Editor of the IEEE TRANSACTIONS ON POWER ELECTRONICS.